Proceedings of the Thirty-fourth (2024) International Ocean and Polar Engineering Conference **www.isope.org**
Rhodes, Greece, June 16–21, 2024

ISBN 978-1-880653-78-4; ISSN 1098-6189

Wall-Modeled Large Eddy Simulation for a Highly Decelerated Axisymmetric Turbulent Boundary Layer

Kangjian He[1], Fuchang Zhou[2], Weiwen Zhao[1], Decheng Wan[1]*

[1] Computational Marine Hydrodynamics Lab (CMHL), School of Naval Architecture, Ocean and Civil Engineering, Shanghai Jiao Tong University, Shanghai, China
[2] Wuhan Second Ship Design and Research Institute, Wuhan, China

[*]Corresponding Author

ABSTRACT

Wall-modeled large eddy simulation (WMLES) is conducted to investigate the turbulent flow over an axisymmetric body of revolution (BOR) at zero angle with the open-source CFD toolkit OpenFOAM. The BOR is composed of an ellipsoidal nose, a cylindrical mid-body, and a 20-degree tail cone, and has a length-to-diameter ratio of 3.17. The Reynolds number is 1.90×10^6 based on the freestream velocity and the length of BOR. The unstructured computational grid is designed to capture the near-wall flow structures. The pressure and skin friction coefficients are compared with available experimental and numerical results in literature to validate the computational method and settings. The evolution of the boundary layer on the tail-cone section is mainly analyzed to discuss the effect of adverse pressure gradient. This research can provide a useful reference for studying complex flows in highly decelerated zone.

KEY WORDS: Wall-modeled large eddy simulation; axisymmetric turbulent boundary layer; flow structures; adverse pressure gradient.

INTRODUCTION

Turbulent boundary layers growing over axisymmetric bodies, such as underwater vehicles and aircraft, are of considerable interest in recent years. Understanding the fundamental flow mechanisms is important due to the direct relevance with structural vibrations and flow noise.

Abundant experiments have been conducted to investigate the physics of an axisymmetric boundary layer. Huang et al., (1992), and Jiménez et al. (2010a, 2010b) conducted experiments to study the flow around the DARPA SUBOFF model with high Reynold number, which is a canonical streamlined body of revolution and has been widely used as the benchmark model in studies on hydrodynamics about underwater vehicles. The flow information about time-averaged quantities and turbulent fluctuations in turbulent boundary layer and wake region was obtained. Balantrapu et al., (2021, 2023) conducted a series of experiments with a body of revolution (BOR). Flow structures and wall-pressure fluctuations under the adverse pressure gradient were mainly analyzed. All of these experiments provide many valuable data to dataset for validation of numerical simulations for high Reynolds number about axisymmetric turbulent boundary layer.

In recent years, numerical simulations have been gradually applied in studying axisymmetric turbulent boundary layer. The Reynolds-averaged Navier–Stokes (RANS) method is usually used due to cost considerations and has shown good performance in capturing time-averaged statistical quantities.(Boger and Dreyer, 2006; Cao et al., 2016; Gao et al., 2018; Pan et al., 2012; Yang and Lohner, 2003; Zhang et al., 2019). As the development of the computational performance and numerical algorithms, large eddy simulation (LES) has been an useful engineering tool for predicting and analyzing unsteady and multiscale turbulent flows. For wall-bounded flows, LES can be divided into two types, wall-resolved large eddy simulation (WRLES) and wall-modeled large eddy simulation (WMLES) based on the strategy of dealing with the flow near the wall. For WRLES, the flows in all regions are directly resolved with LES. WRLES has been conducted to simulate the flow around the DARPA SUBOFF model (Fureby et al., 2016; Kumar and Mahesh, 2018; Liu et al., 2023; Morse and Mahesh, 2021; Posa and Balaras, 2016, 2020). Satisfactory results about not only time-averaged quantities but also turbulent fluctuations were obtained comparing with experimental data. However, due to the requirement of LES to solve more than 80% the turbulent kinetic energy in flow, WRLES tends to be computationally expensive when Reynolds number is high. WMELS resolves the flow in the outer layer of the boundary layer and applies modeling approaches for the flow within the inner layer of the boundary layer. This method extends the application of LES in high Reynolds number flow. Chen et al. (2023) and He et al., (2023) used WMLES to simulate the flow around the DARPA SUBOFF model and validate this method in capturing the flow in pressure gradient. Zhou et al. (2020) conducted the numerical simulation about BOR matched Reynolds number of Balantrapu et al., (2021, 2023). They used WRLES on the stern region and WMLES on the nose and mid-body to reduce the computational cost. They analyzed the space–time characteristics of velocity and pressure fluctuations within the boundary layer of the stern cone. In the previous studies, WMLES with the non-equilibrium wall stress model has not been validated and applied to study the flow around BOR benchmark. In this paper, WMLES with the non-equilibrium wall stress model is used in the all

regions of BOR to validated this method. Otherwise, the flow mechanisms of a highly decelerated axisymmetric turbulent boundary layer are further discussed at matched Reynolds number of Balantrapu et al., (2021, 2023). This work can provide a valuable reference to understand WMLES capabilities in capturing complex flow around axisymmetric geometries.

The paper is organized as follows: Firstly, numerical approach is introduced including wall stress modeling method. Second, details of computational setup are discussed. Then the flow physics about the axisymmetric boundary layer are analyzed. Finally, conclusions are given.

NUMERICAL APPROACH

Governing Equations

In WMLES reported here, unsteady filtered Navier–Stokes equations for incompressible flow are solved as follows:

$$\frac{\partial \tilde{u}_i}{\partial x_i} = 0 , \tag{1}$$

$$\frac{\partial \tilde{u}_i}{\partial t} + \frac{\partial \tilde{u}_i \tilde{u}_j}{\partial x_j} = -\frac{1}{\rho}\frac{\partial \tilde{p}}{\partial x_i} + \nu \frac{\partial^2 \tilde{u}_i}{\partial x_j \partial x_j} + \frac{\partial \tau_{ij}^{\mathrm{SGS}}}{\partial x_j} \tag{2}$$

where i=1,2,3 denotes different spatial coordinates, $\tilde{u}$ and $\tilde{p}$ are filtered velocity and pressure, ρ is the fluid density, and ν is the molecular kinematic viscosity of the fluid. The space and time coordinates are represented by x and t. τ_{ij}^{SGS} is the subgrid-scale (SGS) stress tensor calculated by the SGS model.

SGS Model

The impact of scales smaller than the filtered size is represented through the SGS stress tensor $\tau_{ij}^{\mathrm{SGS}} = 2\nu_{\mathrm{SGS}}\tilde{S}_{ij} + (1/3)\tau_{kk}^{\mathrm{SGS}}\delta_{ij}$, where ν_{SGS} is the SGS eddy viscosity determined by the SGS model. In this study, the wall-adapting local eddy-viscosity (WALE) SGS model, proposed by Nicoud and Ducros (1999), is employed to calculate the SGS eddy viscosity. This SGS model is an eddy viscosity model that retains the simplicity and computational efficiency inherent in traditional algebraic SGS models. It is found that this model can predict accurate asymptotic behaviors near the wall and near the wall, and the eddy viscosity diminishes in laminar regions (Posa and Balaras, 2016). The SGS eddy viscosity in WALE model is calculated as

$$\nu_{\mathrm{SGS}} = (C_w\Delta)^2 \frac{(S_{ij}^d S_{ij}^d)^{3/2}}{(\tilde{S}_{ij}\tilde{S}_{ij})^{5/2} + (S_{ij}^d S_{ij}^d)^{5/4}} \tag{3}$$

where Δ is the mesh filter length scale, C_w is the model constant and is set to 0.325 in this study, S_{ij}^d is the traceless symmetric part of the square of the velocity gradient tensor and $\tilde{S}_{ij}$ is the resolved strain-rate tensor.

Wall Stress Model

In WMLES, Eqs. 1 and 2 are solved on a coarse mesh near the wall, where the stress-carrying eddies in the near-wall region are mostly unresolved. Therefore, the mesh alone cannot denote the sharp velocity gradients and the momentum transport near the wall. This causes the SGS model to produce insufficient levels of modelled stresses. Wall stress model is proposed to compensate for such numerical and modelling errors in the underresolved near-wall region of LES**.** The wall-stress model considers the inner layer in a Reynolds-averaged sense through a thin-layer approach and uses a mixing-length model for the eddy viscosity. The wall-stress model is applied through the thin boundary layer equations (TBLE) as

$$\frac{\partial}{\partial x_2}\left[(\nu + \nu_t)\frac{\partial \overline{u}_i}{\partial x_2}\right] = \frac{1}{\rho}\frac{\partial \overline{p}}{\partial x_i} + \frac{\partial \overline{u}_i}{\partial t} + \frac{\partial \overline{u}_i \overline{u}_j}{\partial x_j} \tag{4}$$

where $i = 1,3$, i.e., wall-parallel directions. ν_t is the eddy viscosity. Terms in the right of TBLE are pressure gradient term, transient term and convective term. TBLE is a partial differential equation. Some terms are usually neglected to simplify this equation as an ordinary differential equation, which is beneficial for solving. If all of these terms are ignored, the wall stress model is called as equilibrium wall stress model (EQWM). If the pressure gradient term is explicitly taken into account while temporal term and convective term are neglected, this model is the so-called non-equilibrium wall stress model (NEQWM). In this paper, NEQWM is adopted. NEQWM can provide better results comparing to EQWM for the flow under the pressure gradient (Chen et al., 2023). It has also been proved that NEQWM can achieve satisfactory results about both time-averaged field and turbulent fluctuations around the axisymmetric turbulent boundary layer (He et al., 2023).

The mode of operation of the wall-stress model includes three main steps. Firstly, values of the velocity and pressure and quantities derived from them such as pressure gradient are sampled a point in the simulation domain. The position of sampled point is set as the center of the third wall-normal mesh around the wall following Chen et al., (2023) and He et al., (2023). The sampled values serve as input to the wall stress model. Second, the local value of the wall shear stress is calculated through the integral of TBLE. Third, the eddy viscosity is corrected on the boundary based on the wall shear stress computed by the wall stress model. More details about the process of wall stress model can also refer to Mukha et al., (2019).

COMPUTATIONAL SETUP

Geometry

The BOR geometry, shown in Fig. 1, consists of an ellipsoidal nose, a constant-diameter (D) cylindrical mid-body, a 2:1 ellipsoidal nose, and a 20-degree tail cone. The constant diameter of the mid-body D is 0.432m and the length of the BOR geometry is L=3.17D. This geometry is a typical axisymmetric body of revolution with both lateral and longitudinal curvatures. Compared with the SUBOFF, the BOR model has a smaller length-to-diameter ratio and a sharp corner between the mid-body and the tail cone. The freestream velocity of fluid u_∞ is 22 m/s and the corresponding Reynolds number $Re_L = \frac{u_\infty L}{\nu}$ is 1.90×10^6. The physical conditions of the present simulations are identical to those of the experiments conducted in Balantrapu et al., (2021, 2023), with the difference that a shaft at the stern was used to support the BOR in experiments.

The boundary layer keeps laminar without tripping. Therefore, the flow is tripped by applying a steady wall-normal velocity perturbation at the same position (x/D = 0.98) as that in experiments (Balantrapu et al., 2021, 2023). It is noted that the experiments conducted in Balantrapu et al., (2021, 2023) used a square trip ring while the simulation used the steady wall-normal velocity of $0.06\,u_\infty$. This will lift the boundary layer and mimics the presence of the trip ring in experiments. This method of tripping has been tested in previous simulations (Kumar and Mahesh, 2018; Morse and Mahesh, 2021), where a small steady wall-normal velocity over few cells quickly induced the transition of an axisymmetric laminar boundary layer into a turbulent state

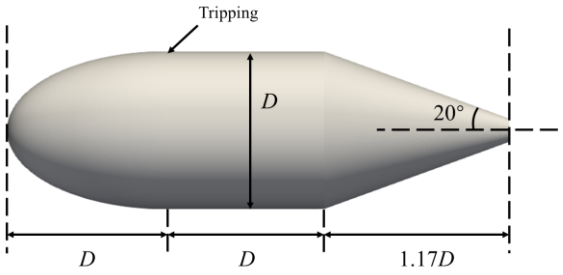

Fig. 1 The BOR geometry

Computational Domain

The schematic of the computational domain is illustrated in Fig. 2. In this study, the half domain is used. It is noted that the all of the body was used in the experiment (Balantrapu et al., 2021). However, the shape of the computational geometry is an axisymmetric body. The computational geometry is fixed and the motion of the body is not considered in this study. Therefore, we used the half domain and symmetry boundary condition in the *xoz* plane to reduce the computation cost. The origin is located at the nose of BOR and the direction of *x*-axis is along the streamwise direction. The *z*-axis is vertically upward and the *y*-axis is determined based on a right-handed coordinate system. The computational domain extends to -12D <y < 0 in the spanwise direction and -12D < z < 12D in the vertical direction. The inlet is located 12D in front of the nose of BOR and the outlet is located 31D downstream of the stern.

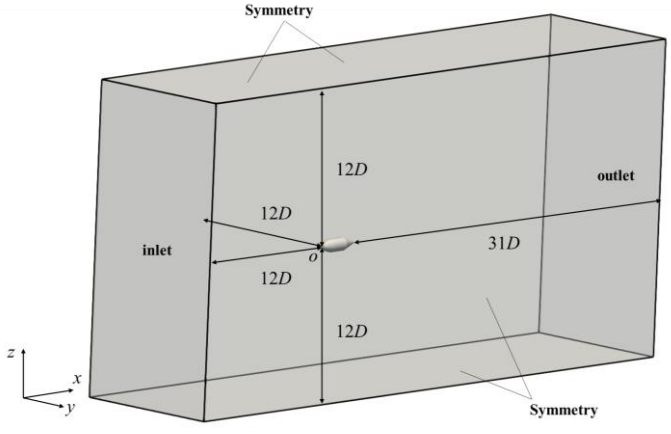

Fig. 2 The schematic of the computational domain

Computational Mesh

The mesh arrangement in *x*-*z* plane and *y*-*z* plane are shown in Fig. 3(a) and (b), respectively. The layout of computational mesh refers to the work of (Chen et al., 2023; He et al., 2023). The unstructured mesh is applied and generated by *snappyHexMesh* in OpenFOAM. The near-wall region is refined to capture the near-wall turbulent structures in the boundary layer. Otherwise, meshes in stern region are also refined to capture the unsteady turbulent flow in adverse pressure gradient. 30 layers are set in the boundary layer region and the boundary layer thickness δ is determined at the end of mid-body based on the experimental results of Balantrapu et al., (2021). The growth ratio of meshes in the boundary layer is 1.03. The size of the first mesh is $\Delta x = \Delta z = 5\Delta y_w = 1/10\delta$. The mesh in the stern boundary layer is shown in Fig. 3(c). Finally, the number of meshes is determined as 37.89 million.

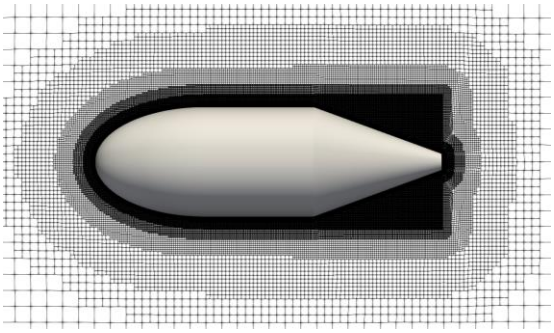

(a) Mesh in the *x*-*z* plane

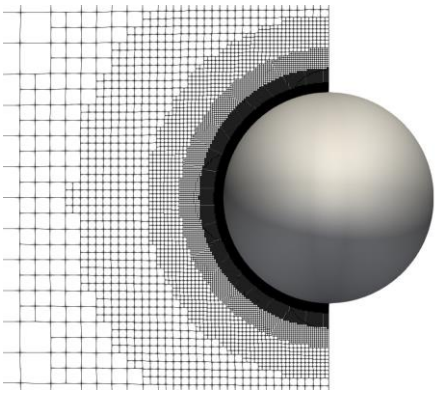

(b) Mesh in the *y*-*z* plane

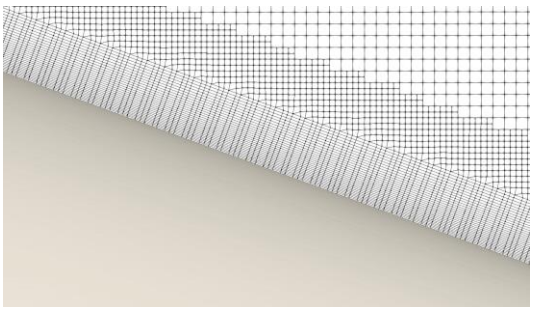

(c) Mesh in the stern boundary layer

Fig. 3 Computational Mesh

Numerical Solution and Schemes

The simulation in this paper is conducted in open-source computational fluid dynamics (CFD) platform OpenFOAM. The simulation is firstly conducted in steady RANS with the solver *simpleFoam* in OpenFOAM. The turbulence model in steady RANS in this paper is $k-\omega$ SST turbulence model. The Semi-Implicit Method for Pressure Linked Equations (SIMPLE) algorithm (Caretto et al., 1973) is used to solve mass and momentum equations. Final convergent solutions of velocity and pressure are obtained as the initial condition of WMLES. WMLES is conducted with the solver *pisoFoam* with the open-source library *libWallModelledLES*(Mukha et al., 2019). Pressure Implicit with Splitting of Operators (PISO) algorithm (Issa, 1986) is used to solve governing equations in the LES simulation.

For LES simulation, second-order implicit backward scheme is used for the temporal discretization. For the spatial discretization, the advection term is discretized with the second-order linear-upwind stabilised transport (LUST) scheme. This scheme blends the linear scheme (75%) and the linear-upwind scheme (25%), which balances the stability and accuracy. The gradient term and laplacian term are discretized using the second-order linear scheme. For the RANS simulation, the advection term in the momentum equation is discretized with second linear scheme. Terms in turbulence transport equations are discretized with upwind scheme. Others are set as same with LES.

Boundary Conditions

In LES simulation, for the inlet boundary, the uniform inflow condition, (u_∞, 0, 0) is used for the velocity boundary condition. The zero normal gradient condition in OpenFOAM is used for the pressure boundary condition. ν_t is calculated from the turbulence model. For the outlet boundary, the zero normal gradient condition is used for the velocity. The fixed value p=0 is used for the pressure boundary condition. ν_t is calculated from the turbulence model. For the boundary of BOR, no-slip boundary condition is used for the velocity and the zero normal gradient condition is used for pressure. ν_t is calculated with NEQWM. For the boundary condition of sides, symmetry boundary condition is adopted.

In RANS simulation, for the inlet boundary condition, the fixed value condition is used for the turbulence kinetic energy and turbulence specific dissipation rate. The turbulent kinematic viscosity is calculated by $k-\omega$ SST turbulence model. For the outlet boundary condition, inletOutlet boundary condition in OpenFOAM is used for the turbulence kinetic energy and turbulence specific dissipation rate. The turbulent kinematic viscosity in the outlet boundary is calculated by $k-\omega$ SST turbulence model. For the boundary of BOR, wall functions are used for turbulence kinetic energy, turbulent kinematic viscosity and turbulence specific dissipation rate. Others are consistent with LES.

Time Step and Solution Time

The time step in this paper is set as 1×10^{-5}s and corresponding nondimensional value is $\Delta t^+ = u_\infty \Delta t / L = 1.6065\times10^{-4}$, satisfying that the maximum Courant number is less than 0.8. The solution time is equal to 24 flow-through times.

RESULTS AND DISCUSSIONS

Overview of the Flow Field

Contours of instantaneous axial velocity nondimensionalized by u_∞, pressure coefficient C_p and vorticity magnitude in *xoz* plane are shown in Fig. 4, which are plotted using Turbulucid (Mukha, 2018). The black solid lines represent the surface of the BOR. The pressure coefficient is defined as

$$C_p = \frac{p - p_\infty}{0.5\rho u_\infty^2} \tag{5}$$

where p_∞ is the reference pressure. The near-wall structures around the BOR, shown in Fig. 5, are identified using the modified normalized Liutex-Omega method (Liu and Yu, 2022; Pang et al., 2023). This method uses isosurface of a normalized scalar $\tilde{\Omega}_R$ to identify vortex structures. The threshold value of isosurface of $\tilde{\Omega}_R$ is set as the recommended value 0.52 (Zhao et al., 2020).

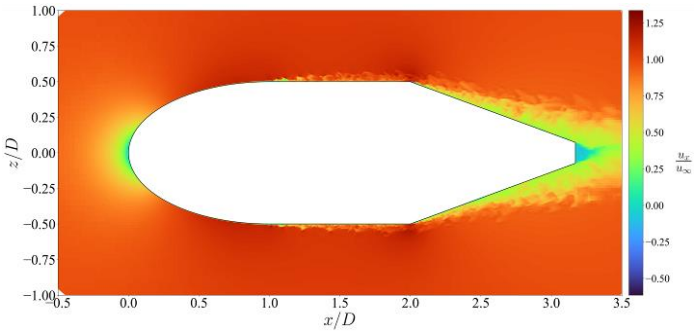

(a) Instantaneous axial velocity nondimensionalized by u_∞

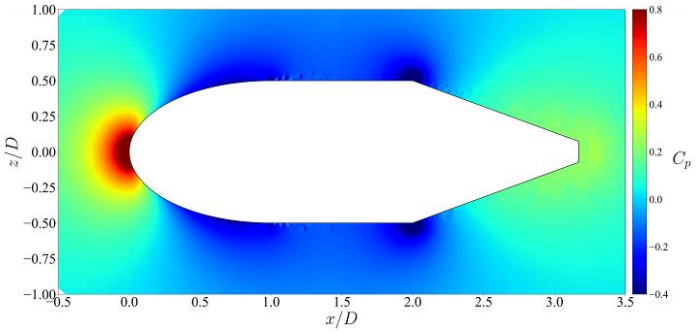

(b) Instantaneous pressure coefficient

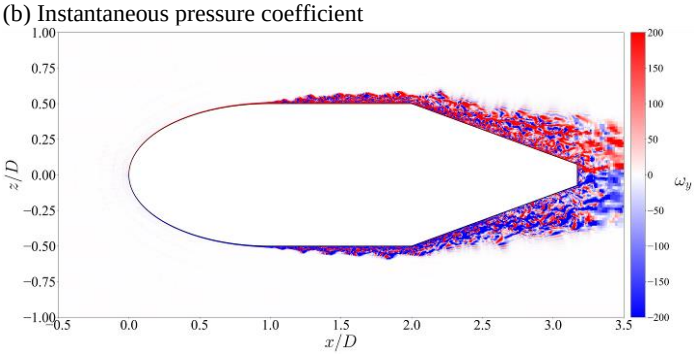

(c) Instantaneous vorticity magnitude

Fig. 4 Contours of instantaneous axial velocity nondimensionalized by u_∞, pressure coefficient C_p and vorticity magnitude in *xoz* plane.

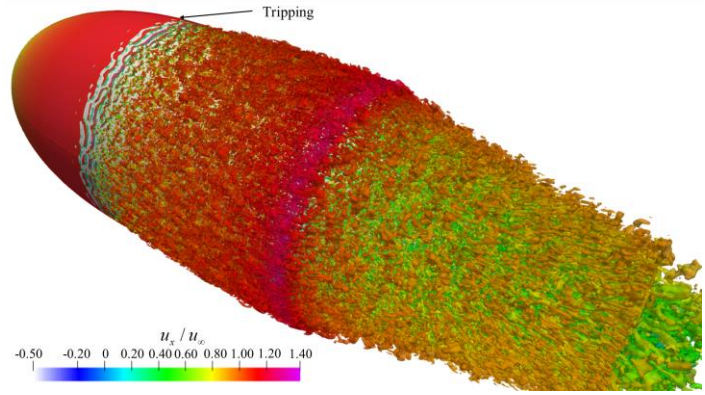

Fig. 5 Near-wall structures around the BOR colored by the axis velocity nondimensionalized by u_∞.

When the fluid flows over the surface of BOR, a stagnation point is firstly formed in the front of the nose. Then the flow is accelerated in the favor pressure gradient as shown in Fig. 4(a). The flow is still laminar until the trip is forced and quickly transition into turbulent. The flow on the short mid-body is mainly the zero-pressure-gradient turbulent boundary layer. The boundary layer is developed and only influenced by lateral curvatures. After that, the flow is influenced by longitudinal curvature at the stern and highly decelerated under the adverse pressure gradient. One can see that the turbulent fluctuations are very strong in the stern region and the vorticity magnitude is high. The vortex structures begin to shed from the stern and form the wake vortices.

Time-averaged Pressure and Skin-friction Coefficients

The streamwise variation of mean pressure along the body is shown in Fig. 6, with the comparison with experimental results (Balantrapu et al., 2021). The pressure coefficient achieved a satisfactory agreement with experimental results. At the trip position, the pressure coefficient drops suddenly due to the wall-normal velocity disturbance. It can be found that the flow experiences highly adverse pressure gradient over the 20-degree tail cone shown in Fig. 6

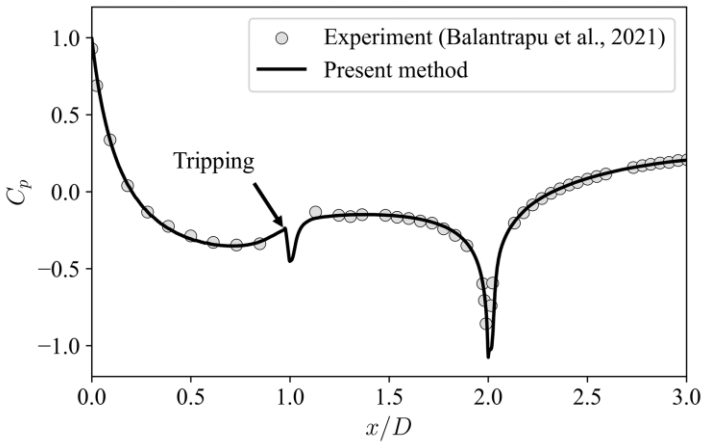

Fig. 6 Comparison of the distribution of time-averaged pressure coefficient with experimental results(Balantrapu et al., 2021).

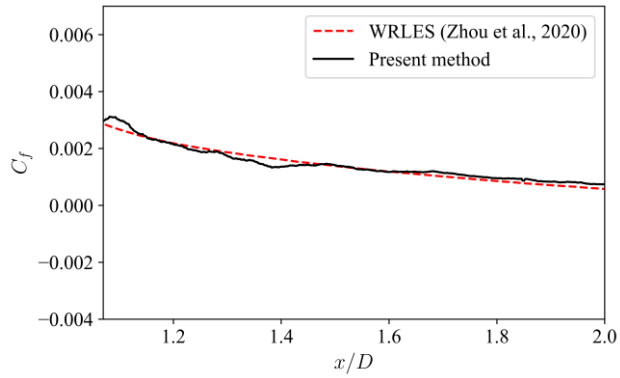

Fig. 7 Comparison of the distribution of time-averaged skin-friction coefficient with previous WRLES results (Zhou et al., 2020).

Distributions of time-averaged skin-friction coefficient on the stern are shown in in and Fig. 7. Available numerical results conducted by WRLES (Zhou et al., 2020) are shown together due to the lack of experimental results. The skin-friction coefficient is defined as

$$C_f = \frac{\tau_w}{0.5\rho u_\infty^2} \tag{6}$$

where τ_w is the magnitude of wall shear stress. Present results agree well with WRLES results, which further validates the numerical method in this paper. The skin-friction coefficient gradually reduces over the stern due to the deceleration of flow.

Evolution of Boundary Layer on the BOR

Fig. 8 shows contours of time-average velocity distribution, which is normalized by u_∞. The traditional definition of the boundary layer thickness ($0.995\,u_\infty$) is not adaptive for this flow b ecause the velocity varies outside of the boundary layer due to longitudinal pressure gradients. Several general methods of determining the boundary layer thickness have been suggested such as the method based on vorticity (Coleman et al., 2018; Spalart and Watmuff, 1993) and total pressure(Patel et al., 1974; Griffin et al., 2021). In this paper, the method based on $0.99\,Cp_{total,\infty}$ is used to calculate the boundary layer thickness. The edge of the boundary layer is represented by the black line as shown in Fig. 8. The boundary layer thickness over the body of BOR is shown in Fig. 9. The boundary layer thickness gradually increases as the flow develops. The boundary layer is mildly lifted at the position of tripping. At the stern, the effect of adverse pressure gradient due to the longitudinal curvature makes the boundary layer thicken quickly. We also show the development of time-averaged axis velocity profiles on the mid-body (Fig. 10) and stern (Fig. 11). The velocity profiles on the mid-body are flatter than those on the stern due to the effect of adverse pressure gradient.

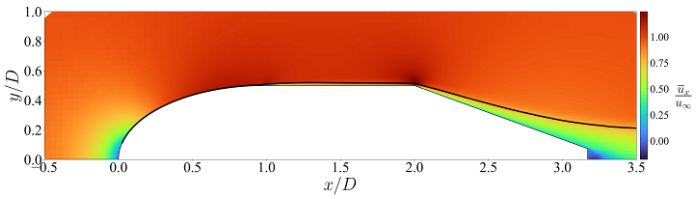

Fig. 8 Contours of time-average velocity distribution and the black line denotes the edge of the boundary layer.

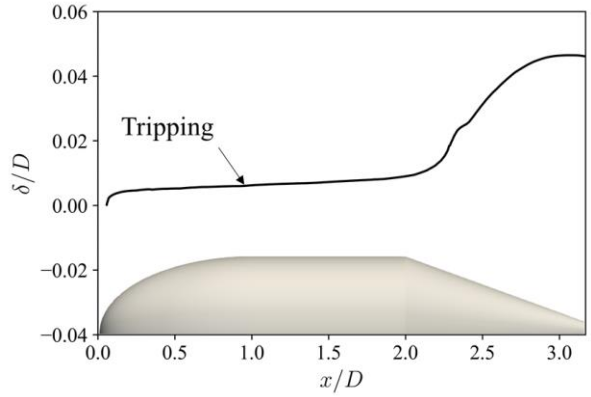

Fig. 9 The evolution of boundary layer thickness over the body.

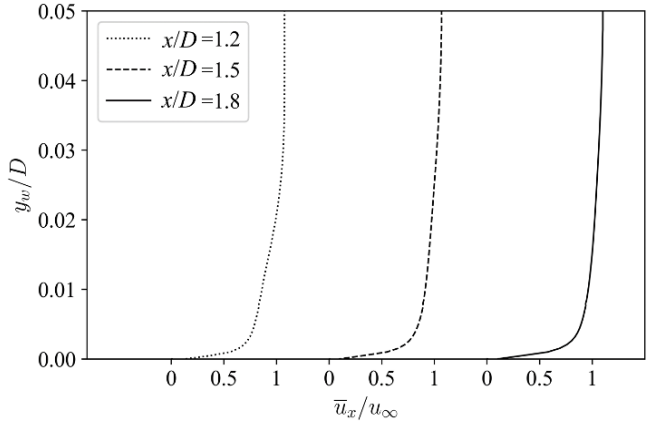

Fig. 10 The evolution of time-averaged axis velocity profiles on the mid-body, normalized by u_∞.

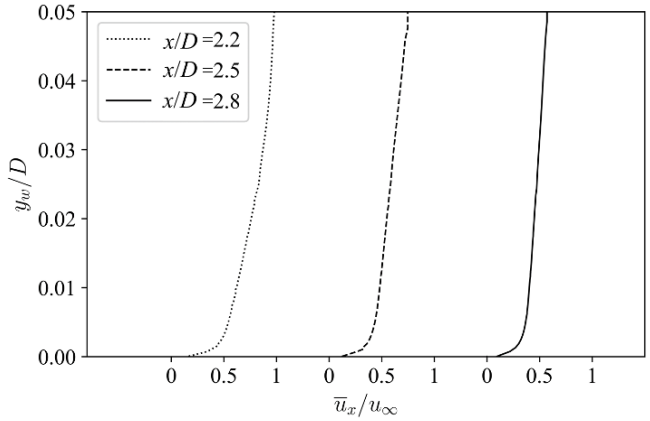

Fig. 11 The evolution of time-averaged axis velocity profiles on the stern, normalized by u_∞.

CONCLUSIONS

In this paper, WMLES is conducted to investigate the flow over an axisymmetric BOR at $Re_L = 1.90\times10^6$. Instantaneous fields and near-wall flow structures are captured. Main characteristics of the flow over the body are analyzed together with the variation of pressure gradient. The pressure and skin friction coefficients achieved great agreements with available experimental and numerical results in literature. The evolution of the boundary layer on the tail-cone section is mainly analyzed. The method base on the total pressure is used to calculate the boundary layer thickness. It is found that the effect of adverse pressure gradient due to the longitudinal curvature makes the boundary layer thicken quickly. Otherwise, the velocity profiles on the mid-body are found flatter than those on the stern due to the effect of adverse pressure gradient.

In this paper, we mainly focused on the time-averaged flow quantities around the body with WMLES. The validation about turbulent fluctuations and wall-pressure fluctuations are not conducted and analyzed in detail due to the space limitation of papers. In the future, more analysis about the turbulent fluctuations and wall-pressure fluctuations about the flow over BOR will be conducted. The capacities of WMLES in capturing pressure fluctuations are further discussed. The space-time characteristic of turbulent flow around the BOR is also valuable to discuss and explore.

ACKNOWLEDGEMENTS

This work is supported by the National Natural Science Foundation of China (52131102), to which the authors are most grateful.

REFERENCES

Balantrapu, NA, Hickling, C, Alexander, WN, and Devenport, W (2021). "The structure of a highly decelerated axisymmetric turbulent boundary layer," *J Fluid Mech*, 929, A9.

Balantrapu, NA, Alexander, WN, and Devenport, W (2023). "Wall-pressure fluctuations in an axisymmetric boundary layer under strong adverse pressure gradient," *J Fluid Mech*, 960, A28.

Boger, D, and Dreyer, J (2006). "Prediction of Hydrodynamic Forces and Moments for Underwater Vehicles Using Overset Grids," *44th AIAA Aerospace Sciences Meeting and Exhibit*, Reno, Nevada, American Institute of Aeronautics and Astronautics.

Cao, L, Zhu, J, and Zeng, G (2016). "Viscous-flow Calculations of Submarine Maneuvering Hydrodynamic Coefficients and Flow Field based on Same Grid Topology," *JAFM*, 9(2), 817–826.

Caretto, LS, Gosman, AD, Patankar, SV, and Spalding, DB (1973). "Two calculation procedures for steady, three-dimensional flows with recirculation," *Proceedings of the Third International Conference on Numerical Methods in Fluid Mechanics*, Berlin, Heidelberg, Springer Berlin Heidelberg, 60–68.

Chen, S, Yang, L, Zhao, W, and Wan, D (2023). "Wall-modeled large eddy simulation for the flows around an axisymmetric body of revolution," *J Hydrodyn*, 35(2), 199–209.

Coleman, GN, Rumsey, CL, and Spalart, PR (2018). "Numerical study of turbulent separation bubbles with varying pressure gradient and Reynolds number," *J Fluid Mech*, 847, 28–70.

Fureby, C, Anderson, B, Clarke, D, Erm, L, Henbest, S, Giacobello, M, Jones, D, Nguyen, M, Johansson, M, Jones, M, et al. (2016). "Experimental and numerical study of a generic conventional submarine at 10° yaw," *Ocean Engineering*, 116, 1–20.

Gao, T, Wang, Y, Pang, Y, Chen, Q, and Tang, Y (2018). "A time-efficient CFD approach for hydrodynamic coefficient determination and model simplification of submarine," *Ocean Engineering*, 154, 16–26.

Griffin, KP, Fu, L, and Moin, P (2021). "General method for determining the boundary layer thickness in nonequilibrium flows," *Phys Rev Fluids*, 6(2), 024608.

He, K, Zhou, F, Zhao, W, Wang, J, and Wan, D (2023). "Numerical analysis of turbulent fluctuations around an axisymmetric body of revolution based on wall-modeled large eddy simulations," *J Hydrodyn*, 35(6), 1041–1051.

Huang, T, Liu, HL, Groves N., Forlini, T., Blanton, J., and Gowing, S.

(1992). “Measurements of Flows over an Axisymmetric Body with Various Appendages in a Wind Tunnel: the Darpa Suboff Experimental Program,” *In Proceedings of the 19th Symposium on Naval Hydrodynamics*, Seoul, Korea, National Academy Press.

Issa, RI (1986). “Solution of the implicitly discretised fluid flow equations by operator-splitting,” *Journal of Computational Physics*, 62(1), 40–65.

Jiménez, JM, Reynolds, RT, and Smits, AJ (2010a). “The Effects of Fins on the Intermediate Wake of a Submarine Model,” *Journal of Fluids Engineering*, 132(3), 031102.

Jiménez, JM, Hultmark, M, and Smits, AJ (2010b). “The intermediate wake of a body of revolution at high Reynolds numbers,” *J Fluid Mech*, 659, 516–539.

Kumar, P, and Mahesh, K (2018). “Large-eddy simulation of flow over an axisymmetric body of revolution,” *J Fluid Mech*, 853, 537–563.

Liu, C, and Yu, Y (2022). “Mathematical foundation of Liutex theory,” *J Hydrodyn*, 34(6), 981–993.

Liu, Y, Wang, H, Wang, S, and He, G (2023). “A cache-efficient reordering method for unstructured meshes with applications to wall-resolved large-eddy simulations,” *Journal of Computational Physics*, 480, 112009.

Morse, N, and Mahesh, K (2021). “Large-eddy simulation and streamline coordinate analysis of flow over an axisymmetric hull,” *J Fluid Mech*, 926, A18.

Mukha, T (2018). “Turbulucid: A Python Package for Post-Processing of Fluid Flow Simulations,” *JORS*, 6(1), 23.

Mukha, T, Rezaeiravesh, S, and Liefvendahl, M (2019). “A library for wall-modelled large-eddy simulation based on OpenFOAM technology,” *Computer Physics Communications*, 239, 204–224.

Nicoud, F, and Ducros, F (1999). “Subgrid-Scale Stress Modelling Based on the Square of the Velocity Gradient Tensor,” *Flow, Turbulence and Combustion*, 62(3), 183–200.

Pan, Y, Zhang, H, and Zhou, Q (2012). “Numerical Prediction of Submarine Hydrodynamic Coefficients using CFD Simulation,” *J Hydrodyn*, 24(6), 840–847.

Pang, B, Yu, Z, Yan, B-W, Wang, Y, and Liu, C (2023). “Identification of vortex boundaries in two-dimensional incompressible flows based on the Liutex-shear interaction,” *J Hydrodyn*, 35(5), 825–831.

Patel, VC, Nakayama, A, and Damian, R (1974). “Measurements in the thick axisymmetric turbulent boundary layer near the tail of a body of revolution,” *Journal of Fluid Mechanics*, 63(2), 345–367.

Posa, A, and Balaras, E (2016). “A numerical investigation of the wake of an axisymmetric body with appendages,” *Journal of Fluid Mechanics*, 792, 470–498.

Posa, A, and Balaras, E (2020). “A numerical investigation about the effects of Reynolds number on the flow around an appended axisymmetric body of revolution,” *Journal of Fluid Mechanics*, 884.

Spalart, PR, and Watmuff, JH (1993). “Experimental and numerical study of a turbulent boundary layer with pressure gradients,” *J Fluid Mech*, 249(1), 337.

Yang, C, and Lohner, R (2003). “Prediction of Flows over an Axisymmetric Body with Appendages,” Busan, Korea.

Zhang, D, Chao, L, and Pan, G (2019). “Analysis of hydrodynamic interaction impacts on a two-AUV system,” *Ships and Offshore Structures*, 14(1), 23–34.

Zhao, W, Wang, J, and Wan, D (2020). “Vortex identification methods in marine hydrodynamics,” *J Hydrodyn*, 32(2), 286–295.

Zhou, D, Wang, K, and Wang, M (2020). “Large-Eddy Simulation of an Axisymmetric Boundary Layer on a Body of Revolution,” *AIAA AVIATION 2020 FORUM*, VIRTUAL EVENT, American Institute of Aeronautics and Astronautics.